WRF and Vertical Nesting: Multi-Scale Resolution of T-REX Measurements

Mohamed Moustaoui, Alex Mahalov, Basil Nichols
Program in Environmental Fluid Dynamics
Department of Mechanical and Aerospace Engineering
Department of Mathematics and Statistics
Arizona State University, Tempe, AZ 85287-1804
alex@taylor.la.asu.edu, mousta66@pearson.la.asu.edu, byn@stokes.la.asu.edu

1. Abstract

Staggered vertical nests have been developed, coupled with the WRF innermost nests. This methodology is applied to the high resolution simulations of field data from the T-REX Campaign of measurements (Terrain-induced Rotor Experiment), Owens Valley, CA, 2006. Our real case WRF simulations are based on initial and boundary conditions from both high resolution T799 L91 ECMWF analysis data and GFS data. Four nests are used: a parent domain with 9 km grid and two WRF nests with 3 km and 1 km grid spacing. 150 vertical levels are used with adjusted sigma-pressure levels for an improved and more uniform resolution around the tropopause and in the lower stratosphere. The innermost WRF nest is coupled in a one way mode with a fourth domain nested both in the horizontal and the vertical (450 staggered vertical levels). For vertical nesting, both lateral and vertical boundary conditions are treated via relaxation zones where the velocity and temperature fields are relaxed to those obtained from the WRF inner nest. We resolve mountain wave breaking, temperature adiabatic layers, intense vertical velocity fluctuations and dynamics of countergradient flows around

2. Introduction

Stratospheric mechanical turbulence (altitudes 10-25km) is characterized by patchy high frequency fluctuations in the stratospheric wind fields and long-lived energetic eddies with a few hundred meters scales in the vertical. The thin Clear Air Turbulence (CAT) layers negatively impact on the effective control, stability and performance of the newest generation of Unmanned Air Vehicles (UAV). While there is a need for real time forecast of these thin stratospheric CAT layers, these cannot be resolved by even the latest generation of Weather Research and Forecasting (WRF) mesoscale meteorological codes. Our goal is to enable forecasting of nonlinear, non-monochromatic inertia-gravity waves with large horizontal wavelengths (few hundred kilometers) which generate thin (few hundred meters) CAT layers. Coupled tropospheric/stratospheric forecasting CAT and Optical Turbulence (OT) layers is a challenge for real time operational forecasting.

High resolution Coupled WRF (Weather Research and Forecasting)/microscale code simulations are carried to predict and characterize stratospheric CAT and OT layers and to examine and parameterize wind-shear and gravity waves evolution under various local atmospheric conditions, their respective modes of instability, morphology and dynamics, and subsequent breakdown into turbulent motion. This information in turn is used to improve prognostic parameterizations of eddy-mixing coefficients and diagnostic parameterizations of mechanical and optical turbulence for the tropopause and lower stratosphere regions in mesoscale codes.

Non-homogeneous, anisotropic turbulence computations require that a large mesh be used to encompass all pertinent multiscales of stratospheric mechanical and optical turbulence. This, coupled with stiff velocity and temperature gradient profiles, presents significant challenges for nesting and adaptive gridding. Our technical approach is based on microscale vertical nesting and adaptive vertical gridding in coupled WRF/microscale codes.

The inner nest of WRF (1km grid in the horizontal, 150 sigma pressure levels in the vertical) is coupled with a sequence of embedded microscale nests, both horizontally and vertically. The fully three-dimensional, compressible Navier-Stokes equations with non-homogeneous stratification (buoyancy) and background rotation (Coriolis) are solved with a stretched, adaptive grid in the vertical. A sequence of embedded innermost microscale nests is then implemented with 333m grid spacing in the horizontal grid; vertically, 450 staggered sigma pressure levels are used for the fourth innermost nest and 750 for the fifth one. An adaptive, staggered grid mesh is used in the vertical; with a denser grid around the tropopause and in the lower stratosphere, this allows for vertical grid spacing down to 25m in the vertical in thin CAT layers where strong turbulent mixing occurs. For nesting, both lateral and vertical boundary conditions are treated via relaxation zones where the velocity and temperature fields are relaxed to those obtained from the WRF inner nest. Temporal discretization uses an adaptive time-split integration scheme resolving high frequency gravity waves. This allows for increased resolution without the time step costs.

This methodology is applied to the simulations of the T-REX Campaign of measurements (Terrain-induced Rotor Experiment), Owens Valley, CA, 2006. Our real case simulations are based on real initial and boundary conditions from high resolution T799 L91 ECMWF analysis data. The embedded microscale nests predict localized shear layers and diagnose stiff gradients of vertical velocity and potential temperature above the tropopause and in the lower stratosphere. We demonstrate that strong mountain waves are refracted through the tropopause with substantial changes of amplitudes, polarization and phases above 10km; then the significant wavelength shortening of these polarized inertia-gravity waves induce thin stratospheric CAT layers. We resolve fully three-dimensional instability mechanisms and turbulent dynamics within these CAT layers.

The TREX campaign represent an important case of turbulent dynamics associated with topographic gravity waves. During this campaign, several radiosondes were launched from the upwind side of Owens Valley. Vertical Profiles of temperature and wind components were measured with high vertical resolution from the ground up to 30km. Many profiles exhibit high temperature and wind wave-like fluctuations in the lower stratosphere, with different vertical wavelengths and localized adiabatic layers where potential temperature gradients are small. For instance, Figure 1 (left panel) shows vertical profiles of potential temperature, eastward and northward wind components, from measurements during T-REX performed by a balloon launched at (36.49 N, 118.84 W) on April 1, 2006 at 7:50 UTC. High activity of mountain waves is evident from these profiles. The potential temperature profile shows many regions above the tropopause (11km) where the vertical gradients are small (i.e. 12km, 14km and 20km). The vertical profile of the square of Brunt Vaisala frequency (Figure 1 right panel) calculated from the potential temperature shows strong inhomogeneities. At the tropopause, we notice a strong increase in stability around 11.2km with values reaching $N^2 = 19 \times 10^{-4} s^{-2}$ and exceeding those usually observed in the stratosphere ($N^2 = 4 \times 10^{-4} s^{-2}$). Above this level, the stability decreases within thin adiabatic layers in the lower stratosphere; and increases again thereafter and reachs a second maximum just below 13km. This laminated structure with layering of local maxima and minima in stability was also observed in other profiles performed during TREX campaign. The structure of these profiles indicates high activity of mountains waves, with complex dynamics involving small and large scales processes as indicated in the profiles presented in Figure 1 that show coexistence of smaller and larger vertical wavelengths. Real case simulations with resolutions that are higher than those used in standard mesoscale codes are required to adequately predict and understand these process. These simulations also show that regions near the tropopause and in the lower stratosphere experience wave breaking events induced by localized convective and shear instabilities. The resulting inhomogeneous changes in stability within short regions have in turn dramatic impacts on mountain wave propagation itself.

Our simulations with embedded microscale nests demonstrate the deep change of nature of these mountain waves when transmitted through the tropopause (around 11-12km). Strong CAT layers are associated with stiff adiabatic layers of potential temperature. These layers have complex streamwise-spanwise structures, are located as low as 13.5km up to 20km and higher in the stratosphere. In between these adiabatic potential temperature layers, we evidence and fully resolve strong countergradient layers of convective instabilities, with locally unstable stratification. This intricate turbulent coexistence of thin alternating layers of sharp positive/negative gradients of potential temperature was not expected nor resolved by previous simulations in the literature, albeit diagnosed in TREX high altitude measurements. The feedback of stiff temperature layers onto highly turbulent patches of vertical velocity presents a challenge to the control of UAV's and other high altitude platforms.

3. Computational Approach

We solve the 3D Flux-Form Fully Compressible Equations for Atmospheric Dynamics (reference to WRF manual goes here). The equations are formulated using a terrain-following pressure coordinate denoted by η and defined as:
$\eta = (p_{dh} - p_{dht})/\mu_d$ where $\mu_d = p_{dhs} - p_{dht}$

where μ_d represents the mass of the dry air in the column and p_{dh}, p_{dht} and p_{dhs} represent the hydrostatic pressure of the dry atmosphere and the hydrostatic pressure at the top and the surface of the dry atmosphere. The formulated moist equations are:

$$\begin{aligned}
\partial_t U + (\nabla \cdot \mathbf{V} u)_\eta + \mu_d \alpha \partial_x p & \\
+ (\alpha/\alpha_d)\partial_\eta p \partial_x \phi &= F_U \quad (1)\\
\partial_t V + (\nabla \cdot \mathbf{V} v)_\eta + \mu_d \alpha \partial_y p & \\
+ (\alpha/\alpha_d)\partial_\eta p \partial_y \phi &= F_V \quad (2)\\
\partial_t W + (\nabla \cdot \mathbf{V} w)_\eta - g[(\alpha/\alpha_d)\partial_\eta p - \mu_d] &= F_W \quad (3)\\
\partial_t \Theta + (\nabla \cdot \mathbf{V} \theta)_\eta &= F_\theta \quad (4)
\end{aligned}$$

$$\partial_t \mu_d + (\nabla \cdot \mathbf{V})_\eta = 0 \quad (5)$$
$$\partial_t \phi + \mu_d^{-1}[(\mathbf{V} \cdot \nabla\phi)_\eta - gW] = 0 \quad (6)$$
$$\partial_t Q_m + (\nabla \cdot \mathbf{V} q_m)_\eta = F_{Q_m} \quad (7)$$

In these equations, $\mathbf{v}(u, v, w)$ is the velocity vector, θ is the potential temperature, p is the pressure, g is the acceleration of gravity, $\phi = gz$ is the geopotential. $\mathbf{V}$ and Θ are coupled velocity vector and potential temperature and are given by: $\mathbf{V} = \mu_d \mathbf{v}$, $\Theta = \mu_d \theta$. The right-hand-side terms F_U, F_V, F_W, and F_θ represent forcing terms arising from model physics, turbulent mixing, spherical projections, and the earth's rotation.

The above governing equations are resolved together with the diagnostic equation for dry inverse density, and the diagnostic relation for the full pressure (vapor plus dry air)

$$\partial_\eta \phi = -\alpha_d \mu_d \quad (8)$$
$$p = p_0 (R_d \theta_m / p_0 \alpha_d)^\gamma \quad (9)$$

In these equations, α_d is the inverse density of the dry air $(1/\rho_d)$ and α is the inverse density taking into account the full parcel density $\alpha = \alpha_d(1 + q_v + q_c + q_r + q_i + ...)^{-1}$ where $q_\star$ are the mixing ratios (mass per mass of dry air) for water vapor, cloud, rain, ice, etc. Additionally, $\theta_m = \theta(1 + (R_v/R_d)q_v) \approx \theta(1 + 1.61 q_v)$, and $Q_m = \mu_d q_m$; $q_m = q_v, q_c, q_i, ...$

Our numerical method uses a time-split integration scheme following Skamarock and Klemp, 1992 and Wicker and Skamarock, 2002. Low-frequency modes that are meteorologically significant are integrated using a third-order Runge-Kutta time integration scheme. High-frequency acoustic modes are integrated implicitly in the vertical with smaller time steps to maintain stability.

The spatial discretization uses a C grid staggering: Normal velocity are staggered one-half grid length from the thermodynamic variables. Advection of vector and scalar fields is in the form of flux divergence, and is performed using the third order Runge-Kutta time-integration scheme. the advection uses a fifth and third order accurate spatial discretization.

Both upper and lateral boundary conditions are nudged within relaxation zones to the finest WRF nest fields including the vertical velocity.

The numerical code is fully parallelized using MPI, and the memory used by the code is optimized so that a number of processors as small as possible is used. The simulations conducted for these studies are performed on the ASC MRSC SGI Altix ”Eagle” platform (2048 INTEL ITANIUM-II processors) and on the NAVY MRSC IBM P5 ”Babbage” platform. The accuracy of the numerical simulation results is confirmed by doubling the numerical resolutions to resolve the fully nonlinear 3D dynamics, and comparing with the lower resolution runs.

Our coupled WRF with microscale vertical nests simulations are conducted for the period from 03/31/2006 00 UTC to 04/2/2006 00 UTC. WRF domains are centered over (36.49 N, 118.8 W). Three WRF domains are used with a horizontal resolution of 15km, 3km and 1 km, and 150 vertical sigma pressure levels. These levels are adjusted for better resolution of the tropopause and the lower stratosphere. WRF simulations are initialized with high resolution ECMWF T799L91 analysis data, 25 km horizontal resolution and 91 vertical levels. Innermost nesting is done using 300 X 300 in the horizontal and 450 vertical levels up to 10 mb. One way horizontal and vertical nestings are implemented with boundary conditions and initialization from 1 km WRF inner nest. A fifth innermost nesting is further done with 720 staggered vertical levels.

These simulations are performed on HPC platforms using different datasets. We effectively use ”*ensemble forecasting*” by comparing simulations using initialization and boundary conditions from ECMWF T799L91 data and from GFS analysis (1 degree horizontal grid spacing).

4 TREX Simulations: effective resolution of adiabatic layers and strong vertical velocity patches

We first present results from the WRF simulations. The simulations are performed with three domains using two-way nesting. They are initialized with both GFS data and high resolution ECMWF T799L91 analysis data. The use of two datasets is in effect ensemble forecasting.

Figure 2 shows topography for the finest WRF domain (1 km horizontal grid) and wind the vector field at 12 km altitude simulated by WRF on April 1, 2006 at 8:00 UTC. The wind directions are dominated by south-westrelies. The black curve superimposed in this figure presents the trajectory of a balloon launched on April 1, 2006 at 7:50 UTC from the location (36.49 N, 118.84 W) in the upstream side of the highest elevation. During the ascent, the balloon drifts north-eastward by the wind, and is found in the downstream side of the highest elevation as it reaches levels above the tropopause (blue dot).

Figure 3 shows a longitude-altitude cross-section for potential temperature and vertical velocity on April 1, 2006 at 8:00 UTC for the finest WRF domain (1 km horizontal grid), obtained by using initialization and boundary conditions from ECMWF T799L91 analysis. These fields shows clear evidence of mountain waves signature, with high activity primarily occurring in the downstream side of the mountain between (x=125km and 250km). Also the phase lines found in potential temperature field exhibit rearward phase tilts that is characteristic of mountrain waves. We notice that these phases depicted in both vertical velocity and potential temperature fields indicate that the waves are refracted as they are transmitted trough the tropopause (11km). Regions with small vertical gradients of potential temperature gradients are found in the lower stratosphere (at x=150 km, z=13.5 km, and x=190 km , z= 13.5 km, and at x=230 km, z= 13 km). These potential temperature adiabatic layers are associated with small patches of high vertical velocity reaching 5 - 9 m/s. Figure 4 shows the same fields as in the previous figure but with the initialization and the boundary conditions taken from GFS analysis. These datasets have horizontal and vertical resolutions that are much lower than those of the ECMWF T799L91 analysis. On the average, the fields simulated by WRF using both data sources show similar patterns with high activity of mountain waves in the stratosphere. This increases the confidence of the reality for these patterns. This is a way of conducting an "*ensemble forecasting*". This way is different from the standard ensemble forecasting, since we use two completely independent dataset instead of using a perturbed initial conditions. We notice however some differences in the details. Vertical velocity patches and adiabatic layers are resolved with a much better resolution when using ECMWF T799L91 analysis. The adiabatic layers found at x=190km and x=230km are not present when using GFS data.

Figure 5 shows longitude-altitude cross-section for potential temperature and spanwise (northward) vorticity for the finest WRF domain (1 km grid) obtained by using ECMWF T799L91 analysis for initialization and boundary conditions. Terrain induced rotor wave is found at x=150 km just above the valley. Patches of strong dipoles with positive and negative spanwise vorticity are found in regions on both sides of potential temperature adiabatic layers (x=150 km, z=13.5 km, and x=190 km , z= 13.5 km, and at x=230 km, z= 13 km). These dipoles are associated with localized regions where the vertical shear of the horizontal wind is strong enough to develop local instabilities that are probably the causes for the formation the adiabatic layers. In deed the Richardson number field obtained from the same simulations (Figure 6) shows patches of low Richardson number indicating strongly mixed layers at the same locations as the adiabatic layers and the rotor waves. These patches are also associated with local shear intensifications (Figure 7).

Next, we show results from innermost microscale nest simulations coupled with WRF. This nest uses initial and boundary condition from the finest WRF nest. This nest uses 300 grid points in horizontal directions and 450 vertical levels. Both upper and lateral boundary conditions are relaxed towards the finest WRF nest fields. Figure 8 shows topography for the innermost microscale nest and the wind vector field at 12 km altitude simulated by the microscale nest on April 1, 2006 at 8:00 UTC. As in WRF simulations, the wind directions are dominated by southwestrelies in agreement with observations. This is a validation of our microscale code. We notice that the relaxation of the wind field is very smooth at the boundaries. Also, regions with strong turbulent flow are found above the valley, towards the south of the balloon trajectory. In these regions the horizontal wind shows strong drag, and the direction of the wind is complex. This turbulent flow is more evident in Figure 9. This figure shows longitude (118.56 W, 117.42 W)-altitude cross-section at latitude 36.82 N for potential temperature (contour) and vertical velocity (color) on April 1, 2006 at 8:00 UTC for the innermost microscale domain (333m grid). The potential temperature shows multiscales patterns with fine structures that are not resolved by the WRF finest nest (Figure 3 and 4). Near the tropopause (12km) a localized layer is found where the potential temperature contours are well packed togother indicating strong local increase in stability. This layer shows a wave-like pattern with horizontal wavelengths as short as 10km near x=40km. This wave cannot be excited directly by topography, since its wavelength is much smaller than the horizontal scale of the mountains, and is not observed in potential temperature below 12 km at upper tropospheric levels (9-10km). This suggests that the wave observed in the high stratification layer is generated locally by nonlinear interactions and/or wave breaking. At some levels above 12 km, there are regions in the lower stratosphere where stratification decreases within adiabatic layers, while other regions show localized stiff gradients. The resulting strong local inhomogeneities in stratification with layering of local maxima and minima are observed during TREX (Figure 1) and have in turn dramatic impacts on wave propagation. High stratifications tends to shorten the vertical wavelength of a propagating wave and tends to increase its horizontal wind amplitude resulting in local unstable regions with high local shear; while adiabatic and convectively unstable layers may develop regions where waves are trapped or even reflected. This complex nonlinear dynamics involving multiscale interactions result in a turbulent flows in the lower stratosphere as depicted in Figure 9, where the wavelength of the topographic wave causing this dynamics is hardly identified (the dominant wavelength of the topographic wave should much the horizontal scale of the mountain). Figure 10 shows longitude-altitude cross-section for potential temperature and spanwise (northward) vorticity from the innermost microscale nest. Terrain induced rotor wave is found above the valley; and patches of strong dipoles with positive and negative spanwise vorticity are observed in regions on both sides of potential temperature adiabatic layers and also on the sides of the stiff gradient regions. Figure 11 and 12 shows longitude(118.56W, 117.42W)-altitude cross-sections from the innermost microscale nest at latitude 36.82N for Richardson number and the shear field respectively. Patches of low Richardson number are well resolved and are found primarily near the ground and at upper levels around the tropopause and in the lower stratosphere. We notice that small scales develop in potential temperature primarily in these regions (Figure 9). These strongly mixed layers are induced by nonlinear interactions that are produced by nonlinear rotor waves near the ground and by wave breaking near the tropopause.

The above results demonstrate how mountain waves induced by topography propagate through the tropopause with polarization experience wavelength shortening in the lower stratosphere. The structure is clearly seen from the finest microscale nest. There are intense wave breaking events above the tropopause resulting in formation of several sharp adiabatic layers. Below adiabatic layers at the tropopause level there are regions of high stability characterized by large vertical gradients of potential temperature. This has been observed in several radiosonde profiles during the TREX campaign of measurements. These regions of inhomogeneous gradients can further impact the propagation and transmission of upward propagating topographic waves. These are strongly 3D nonlinear regimes. As shown above, thin adiabatic layers of potential temperature and strong patches of vertical velocity cannot be resolved even by latest generation of Weather Research and Forecasting (WRF) mesoscale codes. They are resolved by the microscale nests with our coupled WRF-microscale nest simulations. While WRF has been successfully applied and validated for the boundary layer and the middle troposphere, it still needs to be improved for the stratosphere.

This project is being expanded into the analysis of recent stratospheric data sets of interest to the USAF. The main focus is to improve parameterization of non-homogeneous anisotropic shear stratified turbulence at tropopause and in the lower stratosphere for WRF (Weather Research and Forecasting) mesoscale code and Air Force operational codes. Such parameterizations and models for the prognosis of thin CAT layers will ultimately be incorporated into real-time Air Force Operational models and ADA (Atmospheric Decision Aid) codes.

Computations were carried out under the Characterization and Prediction of Stratospheric Optical Turbulence for DoD Directed Energy Platforms Challenge Project (C1W). This work is sponsored by AFOSR contract FA9550-05-1-0047

References

Joseph, B., A. Mahalov, B. Nicolaenko, and K. L. Tse, High resolution DNS of jet stream generated tropopausal turbulence, *Geophys. Res. Lett.*, 30, (10), 10.1029/2003GL017252, 2003

Joseph, B., A. Mahalov, B. Nicolaenko, and K.L. Tse, Variability of turbulence and its outer scales in a nonuniformly stratified tropopause jet, *J. Atmos. Sci.*, 41, 524-537, 2004.

Lane, T. P., J.D. Doyle, R. Plougonven, M.A. Shapiro and R.D. Sharman, Observations and numerical simulations of inertia-gravity waves and shearing instabilities in the vicinity of a jet stream, *J. Atmos. Sci.*, 61, 2692-2706, 2004.

Mahalov, A., M. Moustaoui, and B. Nichols, Characterization and forecasting of stratospheric Clear Air Turbulence (CAT) for Air Force Platforms. *Proceedings, of the HPCMP Users Group Conference, IEEE*, 288-295, 2006.

Mahalov, A., B. Nicolaenko, K.-L. Tse and B. Joseph, Eddy-mixing in jet-stream turbulence under stronger stratification, *Geophys. Research Lett.*, vol. 23, L23111-23115, 2004.

Plougonven, R., H. Teitelbaum and V. Zeitlin, Inertia-gravity wave generation by the tropospheric mid-latitude jet as given by the FASTEX radiosoundings. *J. Geophys. Res.*, 108, 4686, 2003.

Tse, K.L., A. Mahalov, B. Nicolaenko, and H.J.S. Fernando, Quasi-equilibrium dynamics of shear-stratified turbulence in a model tropospheric jet, *J. Fluid. Mech.*, **496**, p. 73-103, 2003.

Wicker, L. J., and W. C. Skamarock, Time Splitting Methods for Elastic Models Using Forward Time Schemes. *Monthly Weather Review*, **130**, 2088-2097, 2002.

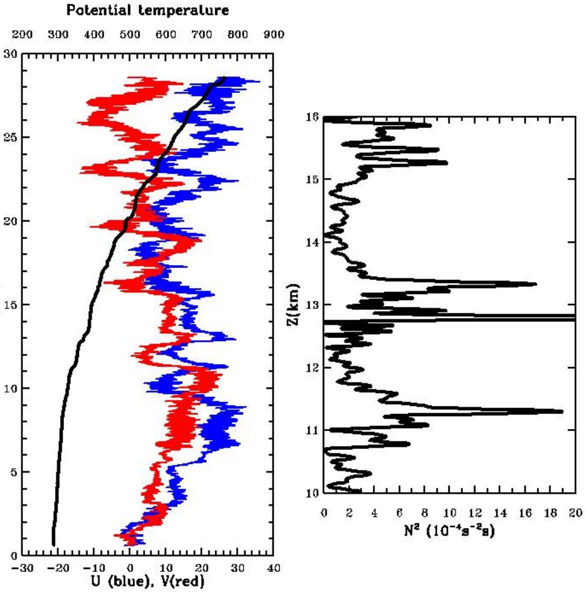

Figure 1. Potential temperature (black), eastward wind (blue), and northward wind (red) from balloon measurments during T-REX. The balloon was launched at (36.49 N, 118.84 W) on April 1, 2006 at 7:50 UTC.

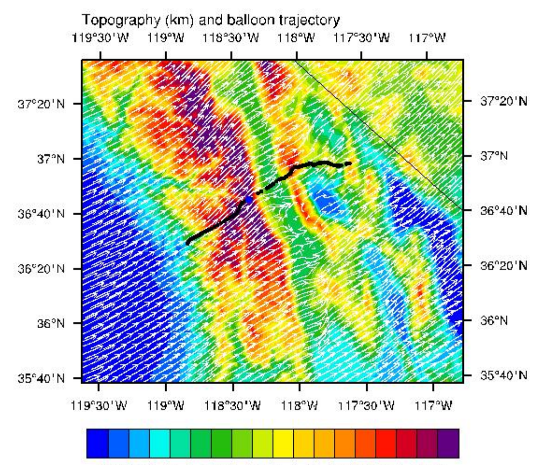

Figure 2. Topography for the finest WRF domain (1 km grid) and wind vector field at 12 km altitude. The black curve shows the trajectory of balloon launched at (36.49 N, 118.84 W) on April 1, 2006 at 7:50 UTC. The blue dot is the location of the balloon at the tropopause

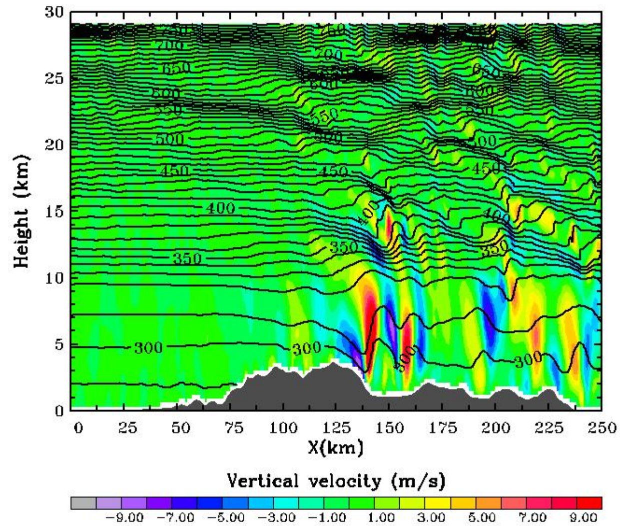

Figure 3. Longitude-altitude cross-section for potential temperature (contour) and vertical velocity (color) for the finest WRF domain (1 km grid) on April 1, 2006 at 8:00 UTC, with ECMWF T799L91 initialization.

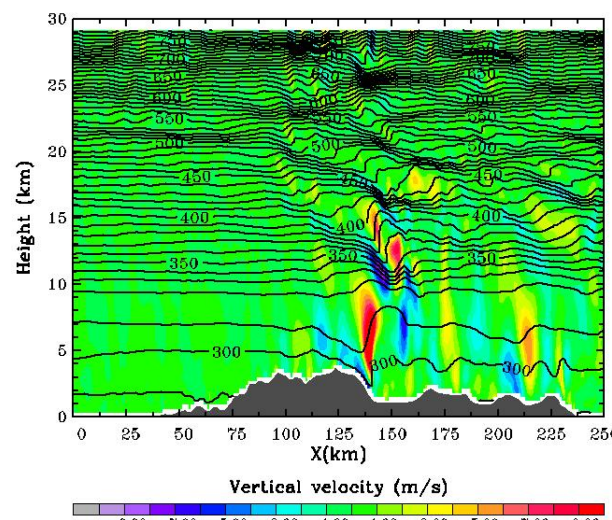

Figure 4. Longitude-altitude cross-section for potential temperature (contour) and vertical velocity (color) for the finest WRF domain (1 km grid) on April 1, 2006 at 8:00 UTC, with GFS initialization.

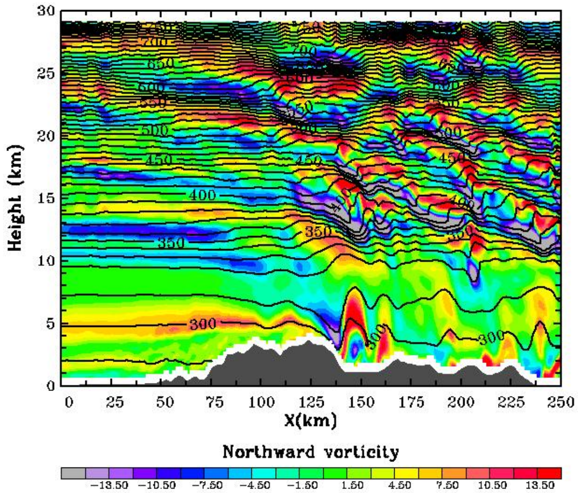

Figure 5. Longitude-altitude cross-section for potential temperature (contour) and span-wise vorticity (color) for the finest WRF domain (1 km grid) on April 1, 2006 at 8:00 UTC, with ECMWF T799L91 initialization.

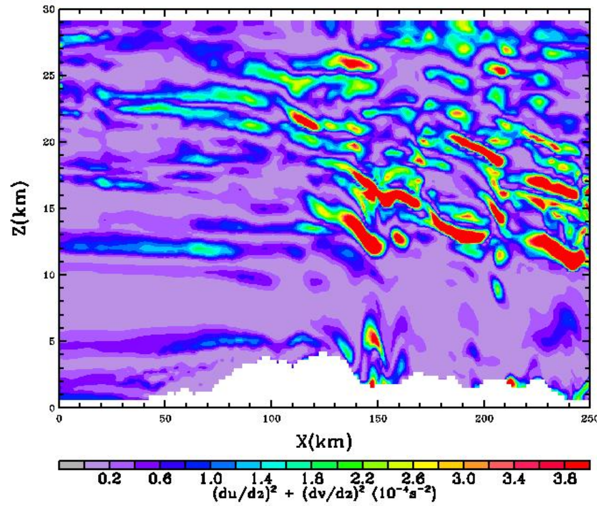

Figure 7. Longitude-altitude cross-section for the square of the shear for the finest WRF domain (1 km grid) on April 1, 2006 at 8:00 UTC, with ECMWF T799L91 initialization.

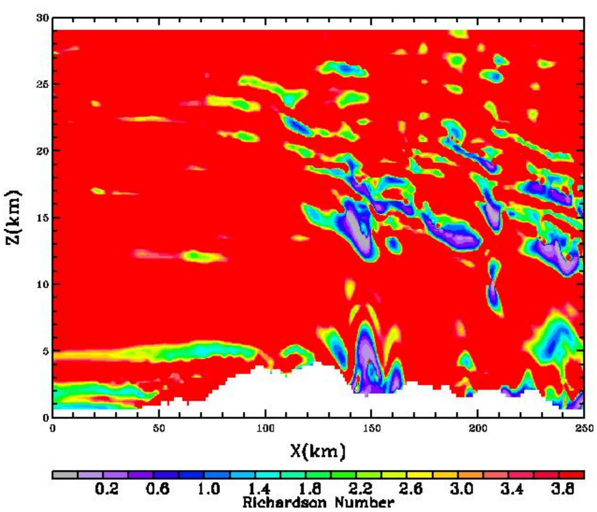

Figure 6. Longitude-altitude cross-section for Richardson number for the finest WRF domain (1 km grid) on April 1, 2006 at 8:00 UTC, with ECMWF T799L91 initialization.

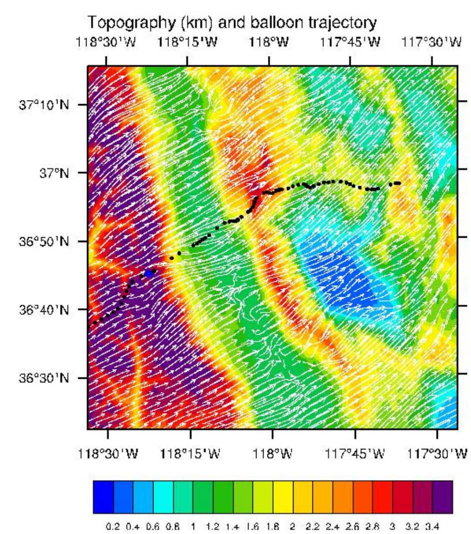

Figure 8. Topography for the innermost microscale nest (333 m grid in the horizontal and 450 vertical levels) and wind vector field at 12 km altitude. The black curve shows the trajectory of balloon launched at (36.49 N, 118.84 W) on April 1, 2006 at 7:50 UTC. The blue dot is the location of the balloon at the tropopause

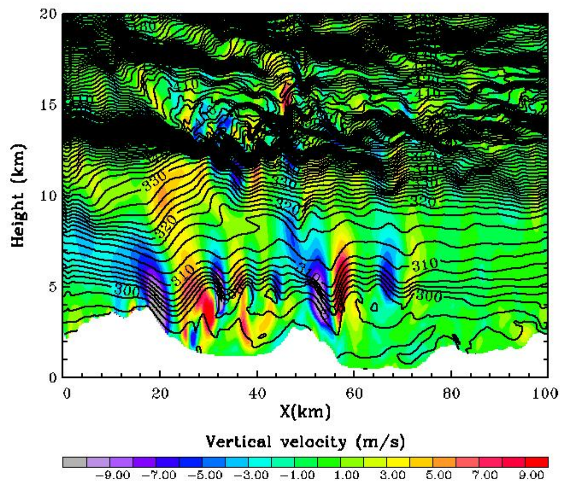

Figure 9. Longitude (118.56 W, 117.42 W)-altitude cross-section at latitude 36.82 N for potential temperature (contour) and vertical velocity (color) for the innermost microscale domain (333m grid); 300 grid points in horizontal directions, 450 vertical levels. The time is 8:00 UTC, April 1, 2006.

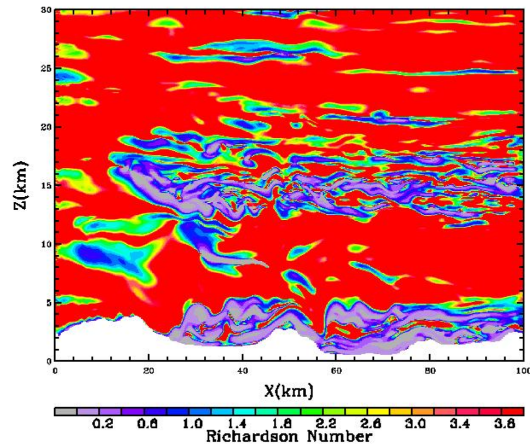

Figure 11. longitude(118.56W, 117.42W)-altitude cross-section at latitude 36.82N for Richardson number for the innermost microscale domain (333m grid); 300 grid points in horizontal directions, 450 vertical levels. The time is 8:00 UTC, April 1, 2006.

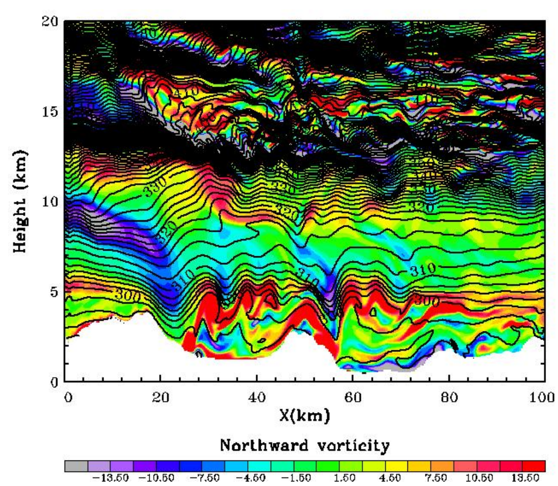

Figure 10. longitude(118.56W, 117.42W)-altitude cross-section at latitude 36.82N for potential temperature (contour) and the spanwise vorticity (color) for the innermost microscale domain (333m grid); 300 grid points in horizontal directions, 450 vertical levels. The time is 8:00 UTC, April 1, 2006.

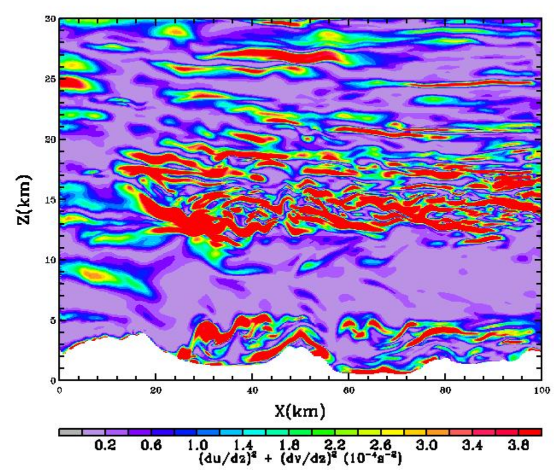

Figure 12. longitude(118.56W, 117.42W)-altitude cross-section at latitude 36.82N for the square of the shear for the innermost microscale domain (333m grid); 300 grid points in horizontal directions, 450 vertical levels. The time is 8:00 UTC, April 1, 2006.